

Ultrafast Synthesis of Transition Metal Phosphides in Air via Pulsed Laser Shock

Ziyuan Xu, Qiao Chen, Xiao Han,* Jiaxuan Wang, Pan Wang, Tao Zheng, Sin-Yi Pang, Jincheng Wang, Hejun Li, Zhenhai Xia, and Jianhua Hao*



Cite This: <https://doi.org/10.1021/acs.nanolett.4c03410>



Read Online

ACCESS |



Metrics & More



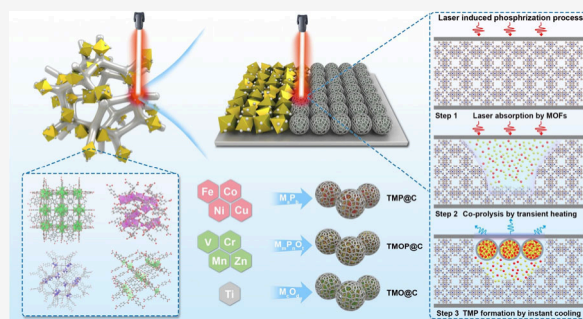
Article Recommendations



Supporting Information

ABSTRACT: Transition metal phosphide nanoparticles (TMP NPs) represent a promising class of nanomaterials in the field of energy; however, a universal, time-saving, energy-efficient, and scalable synthesis method is currently lacking. Here, a facile synthesis approach is first introduced using a pulsed laser shock (PLS) process mediated by metal–organic frameworks, free of any inert gas protection, enabling the synthesis of diverse TMP NPs. Additionally, through thermodynamic calculations and experimental validation, the phase selection and competition behavior between phosphorus and oxygen have been elucidated, dictated by the redox potential and electronegativity. The resulting composites exhibit a balanced performance and extended durability. When employed as electrocatalysts for overall water splitting, the as-constructed electrolyzer achieves a low cell voltage of 1.54 V at a current density of 10 mA cm^{−2}. This laser method for phosphide synthesis provides clear guidelines and holds potential for the preparation of nanomaterials applicable in catalysis, energy storage, biosensors, and other fields.

KEYWORDS: pulsed laser shock, transition metal phosphide nanoparticles, ultrafast synthesis, metal–organic frameworks, electrocatalysis



Transition metal phosphide nanoparticles are of interest in a wide range of applications, including thermal catalysis and electrocatalysis, energy storage, and biosensing/imaging.^{1–3} To develop TMP NPs with well-performed properties, deploying organic/inorganic barriers or overlayers recently appears to be one of the favorable countermeasures, which promises to reconcile high activity with improved stability of compound entities.^{4,5} Metal–organic frameworks (MOFs), a type of organic–inorganic hybrid material with regular porous structures and tunable compositions, have been demonstrated as efficient sacrificial templates and precursors for preparing a series of carbon and transition metal compound nanoparticles (TMC NPs),^{6–8} including transition metal oxides (TMOs),^{9,10} phosphides (TMPs),^{11,12} and oxyphosphides (TMOPs).^{13,14}

To date, most MOF-derived TMP NPs/C nanomaterials have been synthesized through a two-step pyrolysis routine.^{15–17} Carbonization of MOF precursors and incorporation of extraneous anions are included, which are cost- and time-consuming.¹⁸ Moreover, because of mechanical damage caused by the long-term thermal treatment process, immobilizing TMP NPs/C composites to temperature-sensitive metallic substrates (i.e., metal foam) while maintaining their mechanical stability is a daunting task. Therefore, breakthroughs and new synthetic methods based on controllable, cost-effective, and space-limited pyrolysis of MOFs are urgently needed for

preparing TMP NPs/C with adjustable composition, selected phase, and desired catalytic performance.

Several instant heating techniques like joule thermal shock,^{19,20} microwave-assisted heating,^{21,22} flame synthesis,^{23,24} and laser manufacturing^{25,26} recently emerged as time- and cost-effective approaches to replace conventional furnace carbonization. Among them, the laser scribing technique demonstrates its industrial potential in terms of precision, patterning, compatibility, and high-scalability.²⁷ Especially, pulsed CO₂ laser provided by a commercial laser cutter could induce an instantaneously local high temperature to break interatomic bonding and *in situ* produce a reducing atmosphere, which performs as a promising tool to manipulate the synthesis of various nanostructures.^{28–30} However, due to the stringent synthesis conditions of TMPs, reports of TMP NPs synthesized through laser or other rapid synthesis methods are still lacking.^{31,32}

Herein, a time- and power-efficient pulsed laser shock (PLS) method to fabricate MOF-derived core–shell structures with

Received: July 17, 2024

Revised: September 18, 2024

Accepted: September 18, 2024



ACS Publications

© XXXX American Chemical Society

A

<https://doi.org/10.1021/acs.nanolett.4c03410>
Nano Lett. XXXX, XXX, XXX–XXX

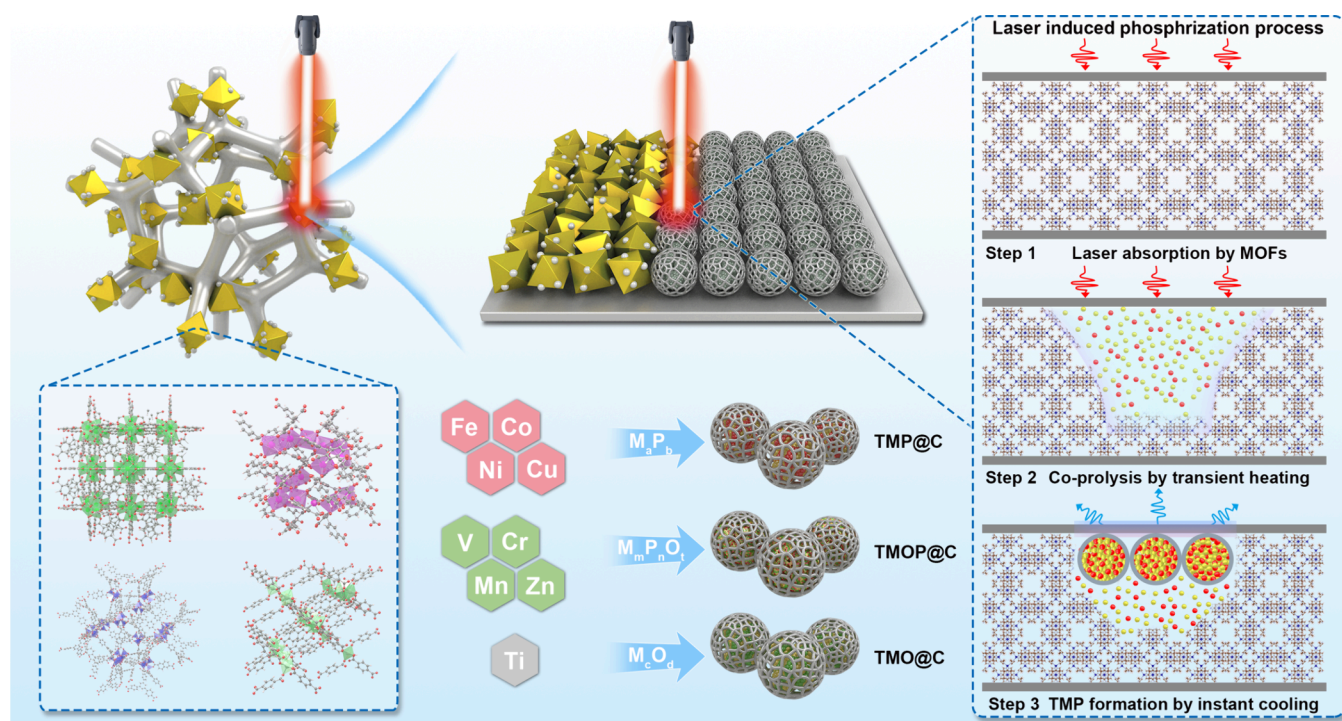


Figure 1. Schematic illustration of the synthesis process of MOF-derived transitional metal phosphide nanoparticles on nickel foam via a pulsed laser shock strategy.

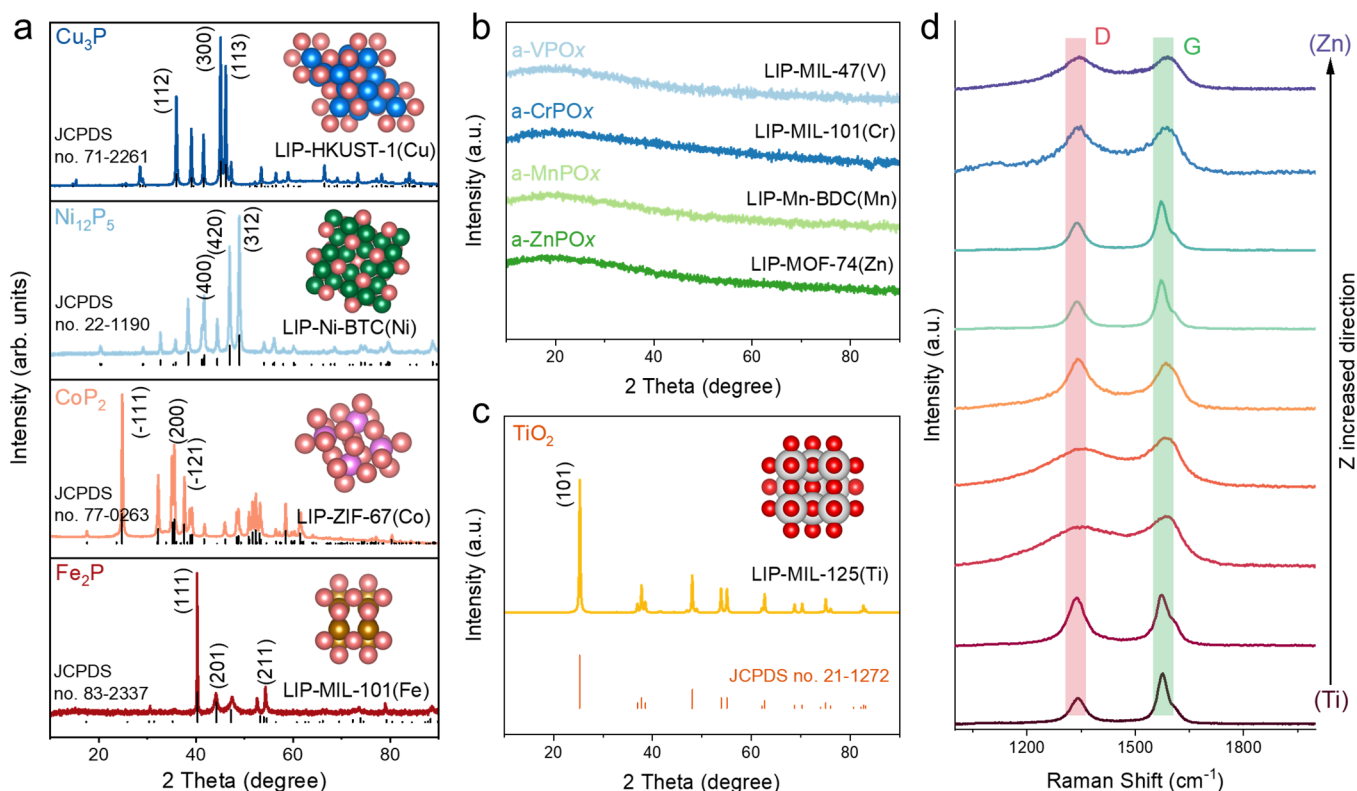


Figure 2. Structural evolution analysis of MOFs under pulse laser shock. (a) PXRD patterns of TMP NPs (TM = Fe, Co, Ni, Cu). (b) PXRD patterns of TMOPs (TM = V, Cr, Mn, Zn). (c) PXRD patterns of TMO NPs (TM = Ti). (d) Raman spectra of LIP-MOFs.

nanosized TMP NPs encapsulated in graphitic carbon is reported. By combination of laser radiation technology and the chemistry of MOFs, the structure and composition of TMP NPs/C can be precisely controlled. The PLS strategy employs

an ultrahigh local temperature and ultrafast heating/cooling rate, thus inducing the fast pyrolysis and recrystallization of MOF precursors without causing thermal damage on the conductive support. In addition, the PLS process could be

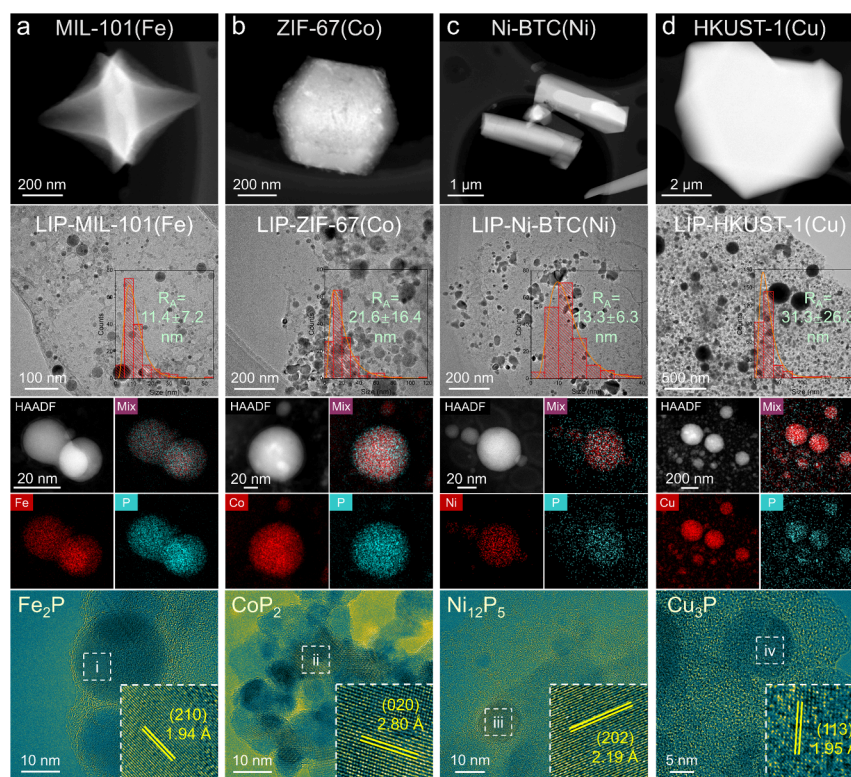


Figure 3. General synthesis of various transition metal phosphides (including iron, cobalt, nickel, and copper) via the PLS strategy. (a–d) TEM characterizations, including BF, HAADF, EDS element mapping, HRTEM images, and corresponding IFFT patterns of (a) LIP-MIL-101(Fe), (b) LIP-ZIF-67(Co), (c) LIP-Ni-BTC(Ni), (d) LIP-HKUST-1(Cu), and their corresponding MOF precursors. The insets are size distributions.

completed within several minutes with several watts of energy consumption, and the strategy here could be extended to synthesize different MOF derivatives.

Figure 1 presents a schematic diagram illustrating the synthesis of LIP-MOFs (LIP: laser-induced phosphorization) on a three-dimensional conductive substrate, specifically nickel foam (NF) or carbon cloth (CC), via the PLS strategy. A variety of MOFs, incorporating different metal ions, were synthesized through a solvothermal method. These include ZIF-8(Zn), HKUST-1(Cu), Ni-BTC(Ni), ZIF-67(Co), MIL-101(Fe), Mn-BDC(Mn), MIL-101(Cr), MIL-47(V), and MIL-125(Ti). The organic linkers employed were chosen based on the specific metal elements, with BDC (Ti, V, Cr, Mn, Fe), BTC (Ni, Cu), DHTA (Zn), and 2-MeIm (Co), as detailed in Table S1.

Following the preloading of MOFs and a phosphorus source onto NF, the PLS process was utilized to convert these precursors into TMC NPs/C heterostructures, referred to as LIP-MOFs. The laser parameters are detailed in Figure S1. Comprehensive characterization techniques were employed to analyze their structure and composition. Figure S2 presents the powder X-ray diffraction (PXRD) patterns of several synthesized representative MOFs, demonstrating a high degree of overlap with ideal MOF crystal structures. SEM images of LIP-MOFs (Figure S2) indicated that post-laser irradiation, the different MOF precursors transformed into similar three-dimensional cross-linked porous composites. Enlarged SEM images (Figure S4–S12) revealed that these composite carbon structures uniformly and firmly adhered to the nickel foam framework, forming a multiscale porous cross-linked structure.

Through PXRD analysis, it was observed that the phase structures after LIP predominantly fall into three categories: (i)

crystalline phosphides for Fe, Co, Ni, and Cu (Figure 2a); (ii) amorphous oxyphosphides for V, Cr, Mn, and Zn (Figure 2b); and (iii) crystalline oxides for Ti (Figure 2c). The PXRD results indicate that not all metals consistently yield phosphide phases under identical laser irradiation conditions. The intrinsic formation mechanisms of these three major products will be further discussed in subsequent sections.

In the process of laser-induced synthesis of TMP nanoparticles, the photothermal effect induced by a laser triggers localized transient high temperatures in the irradiated area,^{28,33} promoting the carbonization of MOF precursors. During this carbonization, the organic linkers and anion sources generate a localized reducing atmosphere, including H_2 , CH_4 , C_2H_4 , and CO.^{34,35} Subsequently, phosphorization occurs with PH_3 produced from the thermal decomposition of sodium hypophosphite, ultimately resulting in the formation of TMP NPs.

In addition to the transformation of metal centers, the Raman spectra in Figure 2d also verify the conversion of organic linkers into graphene structures, which provides robust support for TMP nanoparticles. Although the crystalline/defect degree of graphene is influenced by the intrinsic characteristics of the MOF types, it does not vary with the metal centers. Additionally, during the PLS process, a systematic evolution of the product crystal phase was observed with increasing atomic number, transitioning from oxides to oxyphosphides and subsequently to phosphides. However, this trend does not hold for the element Zn, as depicted in Figure S13. This deviation presents a challenge to developing guiding principles for the selective synthesis of phosphides under PLS conditions.

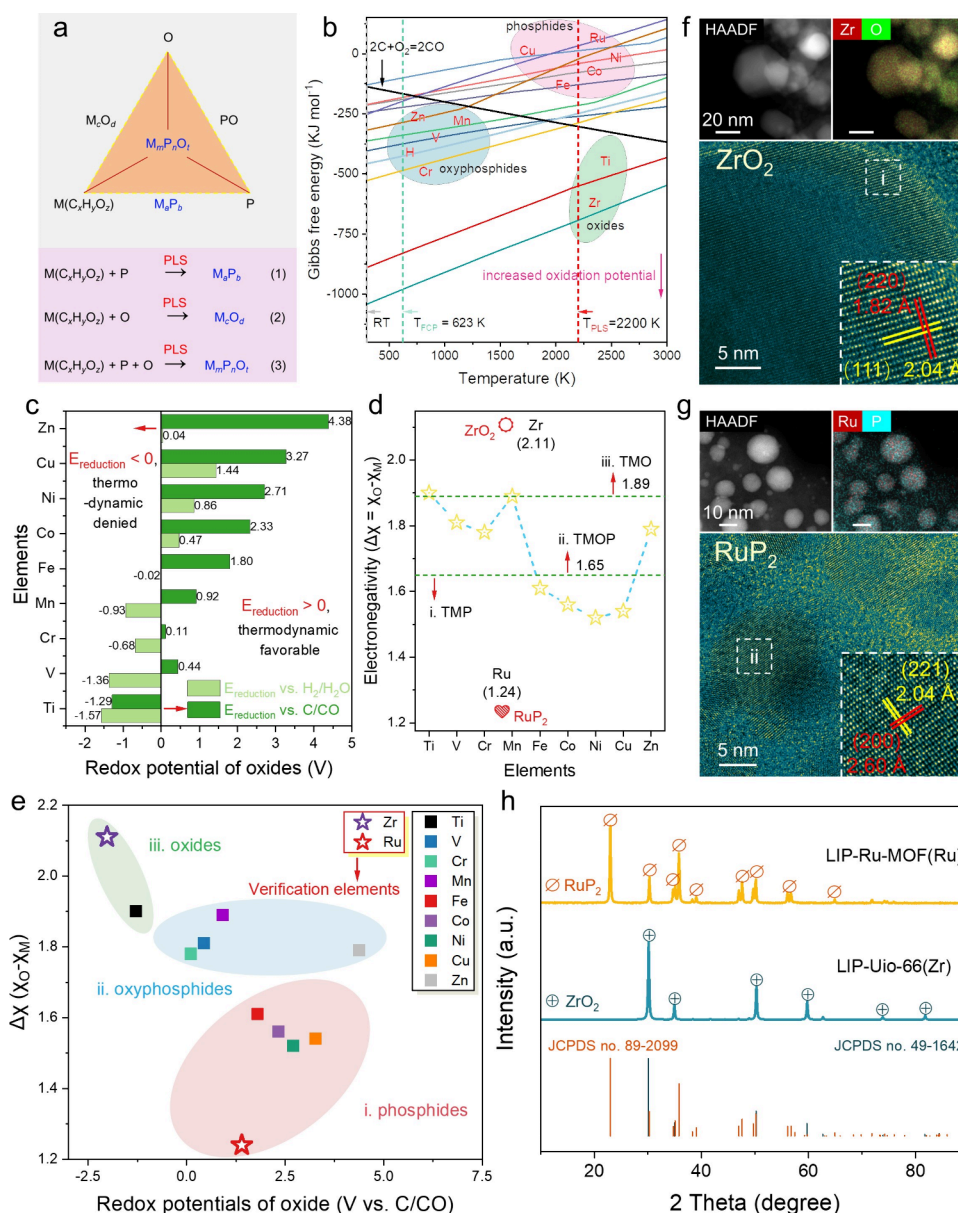


Figure 4. Thermodynamic studies on phase selectivity during the PLS process. (a) Growth phase diagrams of transition metal-based M_3P_b , M_2O_4 , and $M_mP_nO_v$. (b) Ellingham diagram (bulk materials, 1 atm O_2 partial pressure). (c) Electrochemical redox potentials of selective metal oxides (vs C/CO and vs H_2/H_2O). (d) Electronegativity (χ) deviation between oxygen and selected metal elements. (e) Discriminant analysis of obtained phases using electronegativity and redox potentials. Validation test results. (f, g) TEM results, including HAADF-EDS and HRTEM images of (f) LIP-Uio-66(Zr) and (g) LIP-Ru-MOF(Ru). (h) PXRD patterns.

Cs-TEM was employed to characterize the morphology and structural features of the LIP-MOF at a more microscopic scale. As shown in Figures 3a–d, four types of MOF precursors and their laser-irradiated derivatives were studied. TEM images prior to PLS processing indicated that the synthesized MOFs exhibited regular polyhedral morphologies, which transformed into loaded nanoparticles after post-PLS processing. The four types of LIP-MOFs (MIL-101(Fe), ZIF-67(Co), Ni-BTC(Ni), and HKUST-1(Cu)) demonstrated similar characteristics at the micro/nanoscale, featuring uniformly dispersed spherical nanoparticles enveloped by ultrathin carbon layers. Notably, despite undergoing the same PLS process, different TMP NPs exhibited distinct size distributions. The average size (R_A) followed the order $Fe_2P < Ni_{12}P_5 < CoP_2 < Cu_3P$, correlating

with the varying thermal diffusion capabilities of the respective metals.

HAADF and corresponding EDS images confirmed the homogeneous distribution of phosphorus and the corresponding metal elements (Fe, Co, Ni, Cu) in the TMP nanoparticles. In addition to the PXRD results (Figure 2a), HRTEM and SAED provided nanoscale structural information, clearly demonstrating the successful synthesis of TMP nanoparticles via the PLS treatment (Figures 3 and S14). Although the P/M ratio in the precursor was fixed, the resulting phosphides exhibited different P/M ratios within the range of (1/3, 2), encompassing phosphorus-deficient phases (Fe_2P , $Ni_{12}P_5$, and Cu_3P) and phosphorus-rich phases (CoP_2). This variation may be attributed to the higher thermodynamic stability of these phases under PLS conditions.³⁶

The ultrafine size of the TMP nanoparticles can be attributed to the transient high temperatures and ultrafast heating and cooling rates induced by pulse laser irradiation, which prevent Ostwald ripening processes.^{37,38} As the heated region affected by laser irradiation is only at the micro/nanoscale,³⁹ atomic diffusion effects are limited, allowing the reduction atmosphere generated *in situ* to protect TMP from environmental oxidation without the need for additional inert gas as a protective agent. These advantages enable our PLS strategy to synthesize ultrafine TMP nanoparticles with high phase purity.

Although Fe, Co, Ni, and Cu tend to form TMP NPs under PLS conditions, two other types of nanomaterials were also observed: amorphous structures based on V, Cr, Mn, and Zn and oxides based on Ti. TEM results (Figure S15) showed that the corresponding MOF precursors had specific shapes, which transformed into irregular carbonaceous composites after PLS treatment. Unlike the uniformly distributed nanoparticle morphology of TMP NPs/C on the carbon support, the LIP-MOFs (M = V, Cr, Mn, Zn) exhibit a homogeneous distribution of metal, phosphorus, and oxygen elements but lack the uniformly loaded nanoparticles. The uniform distribution of P/O/metals and high O content in the carbonaceous matrix indicated a well-mixed state of elements in the amorphous TMOP phase. By conducting comparative experiments to adjust the ratio of the metal source to the phosphorus source in the precursor (Tables S2 and S3), the broadly tunable Cr/P ratio in the LIP-MIL-101(Cr) was demonstrated, thereby confirming its oxyphosphide structure. Additionally, no obvious lattice fringes were observed in HRTEM images, and the SAED patterns exhibited typical characteristics of amorphous phases, consistent with the PXRD results (Figure 2b).

Combining composition and structural analysis confirmed the structure of amorphous TMOPs, including a-VPO_x, a-CrPO_x, a-MnPO_x, and a-ZnPO_x. Interestingly, unlike the impurities in TMP NPs, nickel species evaporated from the NF substrate ($T_{\text{max}} = 2200 \text{ K} > \text{nickel melting point} = 1728 \text{ K}$, Figure S16) were present as separated nickel-based phosphide nanoparticles in the TMOP/C composites. HRTEM (Figure S17a–c,f,g), HAADF-EDS elemental analysis (Figure S17d), and PXRD pattern (Figure S18) verified the presence of crystalline Ni₁₂P₅ in four LIP-MOFs (M = V, Cr, Mn, and Zn) when using NF as support. Additionally, TEM results (Figures S19 and S20) indicated that the NPs in LIP-MIL-125(Ti) were determined to be TiO₂ doped with phosphorus in a tetragonal crystal structure, consistent with the PXRD results. EPR spectra (Figure S21) showed that a signal peak around $g = 2.001$ can be attributed to unpaired electrons trapped by oxygen vacancies, suggesting a higher oxygen vacancy concentration induced by P doping in TiO₂ nanocrystals from LIP-MIL-125(Ti).

Thermodynamic calculations and validation experiments were conducted to study the phase selection behavior of the LIP-MOFs. Considering the system's exposure to a complex environment containing both P and O, studying the competitive reactions between oxidation and phosphorization was crucial (Figure 4a). Three typical reactions were summarized as follows: R1: $M(\text{C}_x\text{H}_y\text{O}_z) + \text{P} \rightarrow \text{M}_a\text{P}_b$, R2: $M(\text{C}_x\text{H}_y\text{O}_z) + \text{O} \rightarrow \text{M}_c\text{O}_d$, and R3: $M(\text{C}_x\text{H}_y\text{O}_z) + \text{P} + \text{O} \rightarrow \text{M}_m\text{P}_n\text{O}_l$. It was evident that the selectivity of metal elements toward oxidation and phosphorization was critical in

determining whether TMP NPs could be successfully synthesized during the PLS process.⁴⁰

Different metals exhibit varying oxidation potentials $\Delta G_{\text{Oxidation}}$, indicating the difficulty of reducing their oxides to the metallic state. This oxidation potential quantifies the metal's affinity for oxygen.⁴¹ Thermodynamic calculations are extensively employed to predict equilibrium positions within systems, typically neglecting intermediate states. As depicted in Figure 4b, the Ellingham diagram, based on these thermodynamic calculations, reveals the $\Delta G_{\text{Oxidation}}$ and corresponding reduction difficulty for the selected metals' oxides.⁴²

Generally, the elements within the red circle, including Fe, Ni, Co, Cu, and Zn, demonstrate lower levels of oxidation potential, while elements within the blue circle, such as Ti, V, Cr, and Mn, exhibit higher oxidation potentials. This trend aligns well with the phase selectivity among transition metal phosphides, oxyphosphides, and oxides under PLS conditions, although there are exceptions (e.g., Zn). Notably, carbon is commonly used as a high-temperature reducing agent, capable of reducing elements located above the carbon-oxide line (the black line in Figure 4b) through carbothermal reduction. The Ellingham diagram serves as a preliminary guide for the oxidation potentials of different elements.

The ability of various reducing agents to donate electrons to the metal elements within the precursors can be approximated by their electrochemical redox potentials in metal oxides.⁴³ Thermodynamic energy calculations for different oxides were conducted (Figure S22) to evaluate their respective redox potentials ($E_{\text{Reduction}}$) relative to different reducing agents, as illustrated in Figure 4c (vs H₂/H₂O and vs C/CO). For instance, the redox potential for the Cr³⁺/Cr couple at 2200 K is 0.11 V and −0.68 V relative to C/CO and H₂/H₂O, respectively. Consequently, the carbothermal reduction from oxidized Cr to metallic Cr is a spontaneous process, whereas the redox reaction between H₂ and Cr₂O₃ requires additional energy input. Based on the calculated $E_{\text{Reduction}}$ values, the reaction $\text{MO}_n + n\text{C} = \text{M} + n\text{CO}(\text{g})$ is generally more thermodynamically favorable within this system than the reaction $\text{MO}_n + n\text{H}_2(\text{g}) = \text{M} + n\text{H}_2\text{O}(\text{g})$. Therefore, the $E_{\text{Reduction}}$ vs C/CO (carbothermal reduction potential) was determined to be the descriptor for metal oxidation behavior. As shown in Figure S23, there is a good match between the obtained phases and the $E_{\text{Reduction}}$ vs C/CO except Zn. According to the carbothermal reduction potential criterion, MOF-74(Zn) should yield zinc phosphide under laser irradiation, but instead, it forms zinc oxyphosphides, indicating that $E_{\text{Reduction}}$ vs C/CO alone cannot accurately predict the final phase structure.

Figure 4d elucidates a discernible correlation between the deviation in the M–O electronegativity and the resultant phases. Among the selected transition metals, Fe, Co, Ni, and Cu exhibit higher electronegativity values (as depicted in Figure S24), whereas Ti, V, Cr, Mn, and Zn manifest lower values. Generally, metals with diminished electronegativity signify a propensity toward oxygen affinity,⁴⁴ thereby designating Ti, V, Cr, Mn, and Zn as potent deoxidizers.⁴⁵ Typically, as summarized in Figure 4e, transition metals characterized by low $E_{\text{Reduction}}$ and heightened electronegativity tend to yield crystalline phosphides. This observation implies that the intrinsic attributes of the central metal (carbothermal reduction potential and electronegativity) can reliably prognosticate the phase and composition of TMP NPs/C, offering a fundamental design guideline.

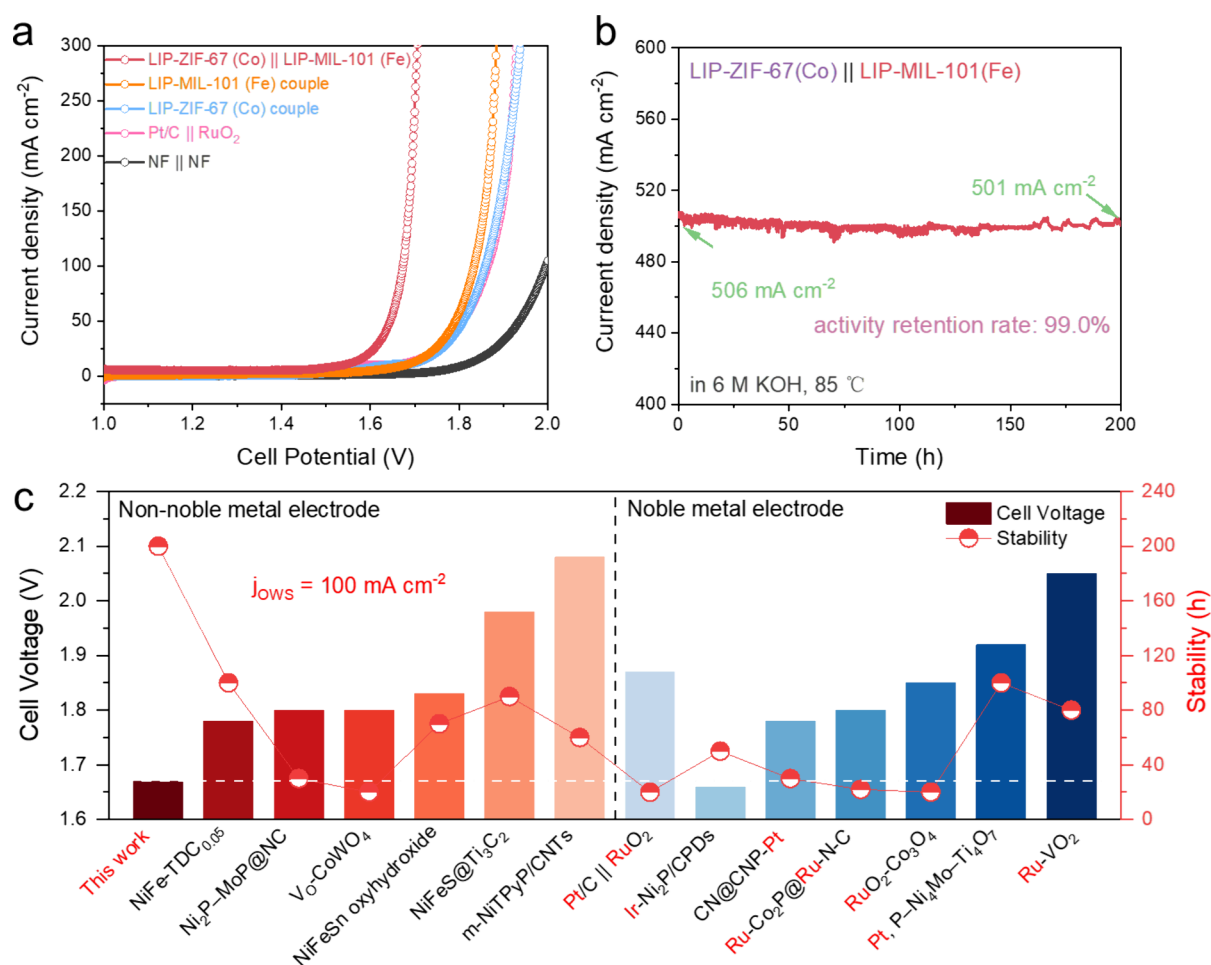


Figure 5. Overall water splitting performance of LIP-MOFs. (a) LSV curves collected using a two-electrode water splitting system. (b) Stability testing via the amperometric i - t technique under a simulated industrial water splitting environment (6 M KOH, 85 °C). (c) Performance and stability contrast to reported advanced water electrolysis systems.

To corroborate the predictability of the established criteria, we selected two additional d-block elements from beyond the first transition series (Zr and Ru) for validation. In accordance with the discriminant analysis outlined in Figure 4e, Zr exhibits a high carbothermal reduction potential ($E_{\text{Reduction}}$ vs C/CO = -2.02 V) alongside a low electronegativity ($\chi = 1.33$), while Ru shows a low carbothermal reduction potential ($E_{\text{Reduction}}$ vs C/CO = 1.40 V) and high electronegativity ($\chi = 2.2$). Consequently, UiO-66(Zr) and Ru-MOF(Ru) are anticipated to undergo transformation into zirconium-based oxide and ruthenium-based phosphides, respectively, following PLS treatment. Subsequent analysis, as delineated in TEM results (Figures 4f,g and Figures S25 and S26) and PXRD patterns (Figure 4h), confirms the phase compositions as cubic ZrO₂ and marcasite-type RuP₂, respectively, in meticulous accordance with the prediction. This empirical validation underscores the accuracy and reliability of the phase selection criteria established in this study.

Transition metal phosphide catalysts derived from MOFs typically demonstrate remarkable electrocatalytic performance in water splitting due to their efficient charge injection and transfer to active sites.^{46–48} In both the hydrogen evolution reaction (HER) and oxygen evolution reaction (OER), LIP-MOFs exhibited superior electrocatalytic activity. To be specific, LIP-ZIF-67(Co) showed HER activity comparable to that of commercial Pt/C catalysts at high current densities,

with overpotentials of 115 mV and 190 mV at current densities of 10 mA cm⁻² and 100 mA cm⁻², respectively (Figure S27). The OER, being a four-electron transfer process, requires more activation energy than its corresponding cathodic reaction, emphasizing the importance of identifying superior OER catalysts.⁴⁹ As illustrated in Figure S28, LIP-MIL-101(Fe) achieved current densities of 10 mA cm⁻² and 100 mA cm⁻² with remarkably low overpotentials of 201 and 232 mV, respectively, surpassing other LIP-MOFs electrodes and RuO₂@NF (313 and 375 mV), as well as other reported advanced electrocatalysts (Table S5). The intrinsic activity of LIP-MOFs was evaluated by calculating the electrochemical double-layer capacitance and turnover frequency values (Figures S29–S31). The LIP-MIL-101(Fe) and LIP-ZIF-67(Co) demonstrated the highest intrinsic activity toward the OER and HER, respectively.

These LIP-MOFs catalysts were utilized as cathodes and anodes to construct an electrolyzer for overall water splitting (OWS) experiments. Compared to other LIP-MOF counterparts and commercial catalysts, the configuration of LIP-ZIF-67(Co) as cathode and LIP-MIL-101(Fe) as anode exhibited the highest activity during OWS. As depicted in Figure 5a, the electrolyzer required voltages of 1.54 and 1.67 V to achieve 10 mA cm⁻² and 100 mA cm⁻², respectively. This performance surpasses the most recent literature reports (Table S6), indicating significantly enhanced catalytic activity. Regarding

long-term stability (Figure S32), the electrolyzer operated at approximately 680 mA cm^{-2} for over 110 h without any decay, outperforming the Pt/C || RuO₂ counterpart.

To investigate the origin of the exceptional stability, we conducted various experiments to study their compositional and structural evolution behavior. Time-dependent ICP-OES measurements (Figure S33) indicated that the total leaching of Fe, Co, and P ions was minimal throughout the reaction (total leaching <1 ppm), and the leaching rates of all ions dropped to very low levels after 50 h, which is consistent with their electrocatalytic stability. Postreaction PXRD and TEM showed that the LIP-ZIF-67(Co) as the cathode maintained its crystalline phase and nanoparticle morphology due to the protection of the encapsulating carbon structure (Figures S34 and S35), while the LIP-MIL-101(Fe) as the anode underwent reconstruction from Fe₂P nanoparticles into goethite α -FeOOH nanorod structures (Figures S36–S38). XPS results (Figure S39) indicate that Fe in Fe₂P exists in a high oxidation state, which may promote the spontaneous reconstruction of Fe₂P during the anodic OER process.

As illustrated in Figure S40, the configuration of LIP-ZIF-67(Co) || LIP-MIL-101(Fe) exhibited multifaceted potential across various electrolytes and maintained outstanding stability over 200 h at an industrial-level current density of 1.65 V under simulated harsh industrial conditions (Figure Sb), indicating its potential for industrial application. As depicted in Figure Sc, the electrolyzer demonstrates performance comparable to, or even surpassing, that of the most advanced transition metal/noble metal-based electrodes in alkaline water electrolyzers. This can be attributed to the confined ultrarapid heating and cooling technique, which induces abundant defects (Figures S41 and S42) within the nanocrystals while minimizing thermal radiation damage to the matrix material.

In conclusion, we have developed a facile, rapid, and energy-efficient PLS technique capable of synthesizing TMP NPs/porous carbon composites within seconds in ambient air. The concurrent pyrolysis of MOF precursors and anionic species facilitates the ultrarapid recrystallization of carbon and the formation of TMPs. This PLS strategy's scalability and versatility were validated through the synthesis of various MOF-derived TMP NPs. Moreover, by integrating experimental results with theoretical analysis, we established a guideline based on electrochemical redox potential and electronegativity for predicting phase selection during the PLS process, providing a directive for subsequent TMP NP synthesis via PLS. We demonstrate the application potential of TMP NPs/C composites toward a water electrolysis system. The proposed PLS strategy enables the controlled and large-scale synthesis of TMP NPs/C on conductive substrates, guided by computational insights, and holds promise for a variety of applications, including electrocatalysis, adsorptive materials, and supercapacitors.

■ ASSOCIATED CONTENT

SI Supporting Information

The Supporting Information is available free of charge at <https://pubs.acs.org/doi/10.1021/acs.nanolett.4c03410>.

Experimental details; XRD patterns of MOF precursors; SEM images, TEM mappings, energy dispersive spectroscopy, SAED patterns, XRD patterns, EPR spectra and XPS spectra of LIP-MOFs; electrochemical testing, stability evaluation, and leaching behavior study of LIP-

MOFs electrodes; XRD patterns, TEM images, HRTEM patterns, and elemental mapping of postreaction LIP-MOFs (PDF)

■ AUTHOR INFORMATION

Corresponding Authors

Xiao Han – State Key Laboratory of Solidification Processing, School of Materials Science and Engineering, Northwestern Polytechnical University, Xi'an 710072, PR China; Chongqing Innovation Center, Northwestern Polytechnical University, Chongqing 401135, PR China; Department of Applied Physics, The Hong Kong Polytechnic University, Hong Kong, PR China; Email: xiao.han@nwpu.edu.cn

Jianhua Hao – Department of Applied Physics, The Hong Kong Polytechnic University, Hong Kong, PR China; orcid.org/0000-0002-6186-5169; Email: jh.hao@polyu.edu.hk

Authors

Ziyuan Xu – State Key Laboratory of Solidification Processing, School of Materials Science and Engineering, Northwestern Polytechnical University, Xi'an 710072, PR China

Qiao Chen – State Key Laboratory of Solidification Processing, School of Materials Science and Engineering, Northwestern Polytechnical University, Xi'an 710072, PR China

Jiaxuan Wang – State Key Laboratory of Solidification Processing, School of Materials Science and Engineering, Northwestern Polytechnical University, Xi'an 710072, PR China

Pan Wang – State Key Laboratory of Solidification Processing, School of Materials Science and Engineering, Northwestern Polytechnical University, Xi'an 710072, PR China; orcid.org/0000-0002-2354-0873

Tao Zheng – State Key Laboratory of Solidification Processing, School of Materials Science and Engineering, Northwestern Polytechnical University, Xi'an 710072, PR China; orcid.org/0000-0001-6817-0899

Sin-Yi Pang – Department of Applied Physics, The Hong Kong Polytechnic University, Hong Kong, PR China

Jincheng Wang – State Key Laboratory of Solidification Processing, School of Materials Science and Engineering, Northwestern Polytechnical University, Xi'an 710072, PR China; orcid.org/0000-0003-2693-9318

Hejun Li – State Key Laboratory of Solidification Processing, School of Materials Science and Engineering, Northwestern Polytechnical University, Xi'an 710072, PR China

Zhenhai Xia – School of Chemical Engineering, University of New South Wales, Sydney, NSW 2052, Australia

Complete contact information is available at:

<https://pubs.acs.org/doi/10.1021/acs.nanolett.4c03410>

Author Contributions

Z.X., Q.C., and X.H. contributed equally to this work.

Notes

The authors declare no competing financial interest.

■ ACKNOWLEDGMENTS

This work was funded by the National Natural Science Foundation of China (52472304, 52002324), Natural Science Foundation of Chongqing (cstc2021jcyj-msxmX0471), Hong Kong Scholars Program (XJ2021073, PolyU YZ4 V), Hong

Kong RGC GRF (PolyU 15301121), and PolyU grant (1-CEOH). We would like to thank the Analytical & Testing Center of Northwestern Polytechnical University for partial support on sample characterizations.

REFERENCES

- (1) Li, S. H.; Qi, M. Y.; Tang, Z. R.; Xu, Y. J. Nanostructured metal phosphides: from controllable synthesis to sustainable catalysis. *Chem. Soc. Rev.* **2021**, *50*, 7539.
- (2) Teymourian, H.; Barfidokht, A.; Wang, J. Electrochemical glucose sensors in diabetes management: an updated review (2010–2020). *Chem. Soc. Rev.* **2020**, *49*, 7671.
- (3) Yang, Y.; Sun, B.; Sun, Z.; Xue, J.; He, J.; Wang, Z.; Sun, K.; Sun, Z.; Liu, H. K.; Dou, S. X. Recent advances and strategies of metal phosphides for accelerating polysulfide redox and regulating Li plating. *Coord. Chem. Rev.* **2024**, *510*, 215836.
- (4) Li, G.; Feng, Y.; Yang, Y.; Wu, X.; Song, X.; Tan, L. Recent advances in transition metal phosphide materials: Synthesis and applications in supercapacitors. *Nano Mater. Sci.* **2024**, *6*, 174.
- (5) Wang, T. J.; Jiang, Y. C.; He, J. W.; Li, F. M.; Ding, Y.; Chen, P.; Chen, Y. Porous palladium phosphide nanotubes for formic acid electrooxidation. *Carbon Energy* **2022**, *4*, 283.
- (6) Wang, X.; Zhang, G.; Yin, W.; Zheng, S.; Kong, Q.; Tian, J.; Pang, H. Metal–organic framework-derived phosphide nanomaterials for electrochemical applications. *Carbon Energy* **2022**, *4*, 246.
- (7) Qian, Y.; Zhang, F.; Zhao, S.; Bian, C.; Mao, H.; Kang, D. J.; Pang, H. Recent progress of metal-organic framework-derived composites: Synthesis and their energy conversion applications. *Nano Energy* **2023**, *111*, 108415.
- (8) Anne Acedera, R.; Theresse Dumlaio, A.; Donn Matienzo, D. J.; Divinagracia, M.; Anne Paraggua, J.; Abel Chuang, P. Y.; Ocon, J. Templated synthesis of transition metal phosphide electrocatalysts for oxygen and hydrogen evolution reactions. *J. Energy Chem.* **2024**, *89*, 646.
- (9) Wei, T.; Zhou, Y.; Sun, C.; Guo, X.; Xu, S.; Chen, D.; Tang, Y. An intermittent lithium deposition model based on CuMn-bimetallic MOF derivatives for composite lithium anode with ultrahigh areal capacity and current densities. *Nano Res.* **2024**, *17*, 2763.
- (10) Yang, G.; Jiao, Y.; Yan, H.; Xie, Y.; Wu, A.; Dong, X.; Guo, D.; Tian, C.; Fu, H. Interfacial engineering of MoO₂-FeP heterojunction for highly efficient hydrogen evolution coupled with biomass electrooxidation. *Adv. Mater.* **2020**, *32*, 202000455.
- (11) Liu, H.; Yang, S.; Ma, J.; Dou, M.; Wang, F. Surface engineering of MOFs as a route to cobalt phosphide electrocatalysts for efficient oxygen evolution reaction. *Nano Energy* **2022**, *98*, 107315.
- (12) Zhang, H.; Chen, A.; Bi, Z.; Wang, X.; Liu, X.; Kong, Q.; Zhang, W.; Mai, L.; Hu, G. MOF-on-MOF-derived ultrafine Fe₂P-Co₂P heterostructures for high-efficiency and durable anion exchange membrane water electrolyzers. *ACS Nano* **2023**, *17*, 24070.
- (13) Babu, D. D.; Huang, Y.; Anandhababu, G.; Ghausi, M. A.; Wang, Y. Mixed-metal–organic framework self-template synthesis of porous hybrid oxyphosphides for efficient oxygen evolution reaction. *ACS Appl. Mater. Interfaces* **2017**, *9*, 38621.
- (14) Yang, L.; Zhang, L. Interfacial electronic modification of bimetallic oxyphosphides as multi-functional electrocatalyst for water splitting and urea electrolysis. *J. Colloid Interface Sci.* **2022**, *607*, 546.
- (15) Shi, Y.; Li, M.; Yu, Y.; Zhang, B. Recent advances in nanostructured transition metal phosphides: synthesis and energy-related applications. *Energy Environ. Sci.* **2020**, *13*, 4564.
- (16) Su, J.; Zhou, J.; Wang, L.; Liu, C.; Chen, Y. Synthesis and application of transition metal phosphides as electrocatalyst for water splitting. *Sci. Bull.* **2017**, *62*, 633.
- (17) Theerthagiri, J.; Murthy, A. P.; Lee, S. J.; Karuppasamy, K.; Arumugam, S. R.; Yu, Y.; Hanafiah, M. M.; Kim, H. S.; Mittal, V.; Choi, M. Y. Recent progress on synthetic strategies and applications of transition metal phosphides in energy storage and conversion. *Ceram. Int.* **2021**, *47*, 4404.
- (18) Cui, X.; Chen, J.; Sun, Z.; Wang, L.; Peng, Q.; Xiao, B.; Zhao, L.; Zheng, H.; Wang, Y.; Wang, J.; Chen, X.; Zhang, Q.; Chen, S. A general route for encapsulating monodispersed transition metal phosphides into carbon multi-chambers toward high-efficient lithium-ion storage with underlying mechanism exploration. *Adv. Funct. Mater.* **2023**, *33*, 22212100.
- (19) Wu, H.; Lu, Q.; Li, Y.; Wang, J.; Li, Y.; Jiang, R.; Zhang, J.; Zheng, X.; Han, X.; Zhao, N.; Li, J.; Deng, Y.; Hu, W. Rapid joule-heating synthesis for manufacturing high-entropy oxides as efficient electrocatalysts. *Nano Lett.* **2022**, *22*, 6492.
- (20) Li, G.; Zhang, W.; Nie, K.; Lv, X.; Deng, J.; Ji, H. Flash Joule heating to enhance water oxidation of hematite photoanode via mediating with an oxidized carbon overlayer. *Carbon* **2023**, *215*, 118444.
- (21) Li, Q.; Gao, J.; Zang, X.; Dai, C.; Zhang, H.; Xin, L.; Jin, W.; Xiao, W.; Xu, G.; Wu, Z.; Wang, L. Synergistic effects of pyrrolic N/pyridinic N on ultrafast microwave synthesized porous CoP/Ni₂P to boost electrocatalytic hydrogen generation. *Inorg. Chem.* **2023**, *62*, 21508.
- (22) Li, Q.; Luan, X.; Xiao, Z.; Xiao, W.; Xu, G.; Li, Z.; Wu, Z.; Wang, L. Ultrafast microwave synthesis of Ru-doped MoP with abundant P vacancies as the electrocatalyst for hydrogen generation in a wide pH range. *Inorg. Chem.* **2023**, *62*, 9687.
- (23) Park, S.; Shin, D.; Yeo, T.; Seo, B.; Hwang, H.; Lee, J.; Choi, W. Combustion-driven synthesis route for tunable TiO₂/RuO₂ hybrid composites as high-performance electrode materials for supercapacitors. *Chem. Eng. J.* **2020**, *384*, 123269.
- (24) Shin, D.; Hwang, H.; Yeo, T.; Park, S.; Kim, T.; Lee, J.; Choi, W. Sol-gel-driven combustion wave for scalable transformation of Mn(NO₃)₂ precursors into MnO_{2-x}/MWCNT supercapacitor electrodes capable of electrochemical activation. *Carbon* **2019**, *152*, 746.
- (25) Pang, B.; Liu, X.; Liu, T.; Chen, T.; Shen, X.; Zhang, W.; Wang, S.; Liu, T.; Liu, D.; Ding, T.; Liao, Z.; Li, Y.; Liang, C.; Yao, T. Laser-assisted high-performance PtRu alloy for pH-universal hydrogen evolution. *Energy Environ. Sci.* **2022**, *15*, 102.
- (26) Lim, H.; Kwon, H.; Kang, H.; Jang, J. E.; Kwon, H. J. Structural isomers: small change with big difference in anion storage. *Nano-Micro Lett.* **2024**, *16*, 13.
- (27) Cui, X.; Liu, Y.; Chen, Y. Ultrafast micro/nano-manufacturing of metastable materials for energy. *Natl. Sci. Rev.* **2024**, *11*, nwae033.
- (28) Zhang, W.; Li, R.; Zheng, H.; Bao, J.; Tang, Y.; Zhou, K. Laser-assisted printing of electrodes using metal–organic frameworks for micro-supercapacitors. *Adv. Funct. Mater.* **2021**, *31*, 2009057.
- (29) Jiang, H.; Jin, S.; Wang, C.; Ma, R.; Song, Y.; Gao, M.; Liu, X.; Shen, A.; Cheng, G. J.; Deng, H. Nanoscale laser metallurgy and patterning in air using MOFs. *J. Am. Chem. Soc.* **2019**, *141*, 5481.
- (30) Tang, Y. J.; Zheng, H.; Wang, Y.; Zhang, W.; Zhou, K. Laser-induced annealing of metal–organic frameworks on conductive substrates for electrochemical water splitting. *Adv. Funct. Mater.* **2021**, *31*, 2102648.
- (31) Liu, Q.; Chen, S. W. Ultrafast synthesis of electrocatalysts. *Trends Chem.* **2022**, *4*, 918.
- (32) Hu, X.; Zuo, D.; Cheng, S.; Chen, S.; Liu, Y.; Bao, W.; Deng, S.; Harris, S. J.; Wan, J. Ultrafast materials synthesis and manufacturing techniques for emerging energy and environmental applications. *Chem. Soc. Rev.* **2023**, *52*, 1103.
- (33) Wu, Y.; Huang, Z.; Jiang, H.; Wang, C.; Zhou, Y.; Shen, W.; Xu, H.; Deng, H. Facile synthesis of uniform metal carbide nanoparticles from metal–organic frameworks by laser metallurgy. *ACS Appl. Mater. Interfaces* **2019**, *11*, 44573.
- (34) Hu, H.; Li, Q.; Li, L.; Teng, X.; Feng, Z.; Zhang, Y.; Wu, M.; Qiu, J. Laser irradiation of electrode materials for energy storage and conversion. *Matter* **2020**, *3*, 95.
- (35) Chen, W.; Salvatierra, R. V.; Ren, M.; Chen, J.; Stanford, M. G.; Tour, J. M. Laser-induced silicon oxide for anode-free lithium metal batteries. *Adv. Mater.* **2020**, *32*, 2002850.
- (36) Liyanage, I. A.; Flores, A. V.; Gillan, E. G. Tunable synthesis of metal-rich and phosphorus-rich nickel phosphides and their

comparative evaluation as hydrogen evolution electrocatalysts. *Inorg. Chem.* **2023**, *62*, 4947.

(37) Yao, Y.; Huang, Z.; Xie, P.; Lacey, S. D.; Jacob, R. J.; Xie, H.; Chen, F.; Nie, A.; Pu, T.; Rehwoldt, M.; Yu, D.; Zachariah, M. R.; Wang, C.; Shahbazian-Yassar, R.; Li, J.; Hu, L. Carbothermal shock synthesis of high-entropy-alloy nanoparticles. *Science* **2018**, *359*, 1489.

(38) Hu, T.; Li, P.; Zhang, W.; Ye, Y.; Liu, J.; Cai, Y.; Zhang, G.; Dai, K.; Liang, C. Laser irradiation induced platinum-based bimetallic alloy nanoparticles in liquids for electrocatalytic hydrogen production. *J. Alloys Compd.* **2023**, *934*, 167914.

(39) Lim, H.; Kwon, H.; Kang, H.; Jang, J. E.; Kwon, H. J. Laser-induced and MOF-derived metal oxide/carbon composite for synergistically improved ethanol sensing at room temperature. *Nano-Micro Lett.* **2024**, *16*, 113.

(40) Chen, F.; Zhao, B.; Sun, M.; Liu, C.; Shi, Y.; Yu, Y.; Zhang, B. Mechanistic insight into the controlled synthesis of metal phosphide catalysts from annealing of metal oxides with sodium hypophosphite. *Nano Res.* **2022**, *15*, 10134.

(41) Yao, Y.; Huang, Z.; Hughes, L. A.; Gao, J.; Li, T.; Morris, D.; Zeltmann, S. E.; Savitzky, B. H.; Ophus, C.; Finck, Y. Z.; Dong, Q.; Jiao, M.; Mao, Y.; Chi, M.; Zhang, P.; Li, J.; Minor, A. M.; Shahbazian-Yassar, R.; Hu, L. Extreme mixing in nanoscale transition metal alloys. *Matter* **2021**, *4*, 2340.

(42) Lam, D. V.; Sohail, M.; Nguyen, V. T.; Ngo, Q. T.; Antoj Jeffery, A.; Choi, H. S.; Jung, N.; Kim, J. H.; Kim, H.; Lee, S. M. Laser-scribed ultrasmall nanoparticles with unary and binary phases. *Chem. Eng. J.* **2021**, *421*, 127731.

(43) Li, Y.; Shao, H.; Lin, Z.; Lu, J.; Liu, L.; Duployer, B.; Persson, P. O. Å.; Eklund, P.; Hultman, L.; Li, M.; Chen, K.; Zha, X. H.; Du, S.; Rozier, P.; Chai, Z.; Raymundo-Piñero, E.; Taberna, P. L.; Simon, P.; Huang, Q. A general Lewis acidic etching route for preparing MXenes with enhanced electrochemical performance in non-aqueous electrolyte. *Nat. Mater.* **2020**, *19*, 894.

(44) Parr, R. G.; Szentpály, L. V.; Liu, S. Electrophilicity Index. *J. Am. Chem. Soc.* **1999**, *121*, 1922.

(45) Han, L.; Cheng, H.; Liu, W.; Li, H.; Ou, P.; Lin, R.; Wang, H. T.; Pao, C. W.; Head, A. R.; Wang, C. H.; Tong, X.; Sun, C. J.; Pong, W. F.; Luo, J.; Zheng, J. C.; Xin, H. L. A single-atom library for guided monometallic and concentration-complex multimetallic designs. *Nat. Mater.* **2022**, *21*, 681.

(46) Jang, K.; Yoon, H.; Hyoung, J. S.; Pratama, D. S. A.; Lee, C. W.; Kim, D. W. Enhancement of hydrogen evolution activity by tailoring the electronic structure in ruthenium-heteroatom-doped cobalt iron phosphide nanoframes. *Appl. Catal., B* **2024**, *341*, 123327.

(47) Wang, Z. M.; Hong, Q. L.; Wang, X. H.; Huang, H.; Yu, C.; Li, S. N. RuP nanoparticles anchored on N-doped graphene aerogels for hydrazine oxidation-boosted hydrogen production. *Acta Physico-Chimica Sinica* **2023**, *39*, 2303028.

(48) Quan, L.; Jiang, H.; Mei, G.; Sun, Y.; You, B. Bifunctional electrocatalysts for overall and hybrid water splitting. *Chem. Rev.* **2024**, *124*, 3694.

(49) Zhang, J.; Yang, H. B.; Zhou, D.; Liu, B. Adsorption energy in oxygen electrocatalysis. *Chem. Rev.* **2022**, *122*, 17028.